Research of near-wall thermodynamic state for indoor airflow over the vertical heating unit using TIV/PIV/RTD

Article

Accepted Version

It is advisable to refer to the publisher's version if you intend to cite from the work. See Guidance on citing.

To link to this article DOI: http://dx.doi.org/10.1016/j.buildenv.2019.106406

Publisher: Elsevier

www.reading.ac.uk/centaur

CentAUR

Central Archive at the University of Reading

Reading's research outputs online

1
2

Research of near-wall thermodynamic state for indoor airflow over the vertical heating unit using TIV/PIV/RTD

3

Qing Wu [a, b], Zhiwen Luo [c,*], Jing Liu [a, b,*]

4
5
6
7

[a] *School of Architecture, Harbin Institute of Technology, Harbin 150000, China.*
[b] *Key Laboratory of Cold Region Urban and Rural Human Settlement Environment Science and Technology, Ministry of Industry and Information Technology, Harbin 150000, China.*
[c] *School of the Built Environment, University of Reading, UK*

8

9

Abstract: Up to now, few studies focus on thermodynamic state including the velocity and

10

temperature of the air near heating unit. The thermodynamic state of the airflow over an indoor

11

heating unit has a significant influence on indoor thermal comfort and energy consumption. This

12

study analyzed the thermal and dynamic state of the near-wall airflow over the heating unit. The

13

thermal state was measured using resistance thermal detectors (RTDs). The near-wall airflow field

14

were measured by particle image velocimetry (PIV) and TIV. The performance of TIV in natural

15

and mixed convection were evaluated by comparing the TIV and PIV measurement results. Under

16

natural convection, the velocity shows vertical variation and the spatial difference changes more

17

pronounced with the increase of heating temperature. Under mixed convection, the near-wall

18

temperature changes uniform and the velocity exhibits a decreasing trend with the increase of

19

height. Through the spectrum analysis of the temperature, it is found that the velocity measured by

20

TIV is close to the velocity near the boundary layer to some content. The positions of the

21

near-surface velocity measured by TIV are not fixed in all cases and change with the change of the

22

boundary layer. The findings in this study can provide a convenient and feasible flow field

23

measurement method suitable for actual space scale. This method can predict the effect of heating

24

terminal units on indoor airflow and thermal environment, so as to optimize the form and

25

arrangement of the heating terminal units, and improve heating efficiency and occupants' thermal

26

comfort.

27

Keywords: Indoor velocity measurement; Near-wall airflow; Temperature distribution; Heating

28

unit; Thermal image velocimetry

*Corresponding author: Jing Liu, Zhiwen Luo
Address: School of Architecture, Harbin Institute of Technology, No.66, Xidazhi Street, Nangang District, Harbin 150000, China (J. Liu).
Tel./fax: +86 0451 8628 2123.
E-mail: liujinghit0@163.com (J. Liu), z.luo@reading.ac.uk (Z. Luo).

1. Introduction

Indoors, due to natural convection, thermal plumes are formed in the vicinity of conventional vertical heating units such as panel or column radiators. In recent years, to improve the thermal efficiency of a typical vertical heating unit, some researchers imposed ventilation to heating units and analyzed the performance of the ventilation heating unit [1][2]. Under this circumstance, the flow process of the airflow over the vertical heating unit can be described as natural or mixed convection. Although the effect of influencing factors such as the surface temperature [3], the location of heating unit [4], the shape of heating unit [5], and the ventilation condition [1][2] on the distribution of indoor environmental parameters such as air temperature and air velocity in the room, have been systematically analyzed. Most of the previous studies have focused on the distributions of indoor air velocity and air temperature, and few studies have focused on the thermodynamic state near the heating unit yet. The flow and the corresponding heat transfer around the surface of heating unit are important factors that determine the distributions of indoor air velocity and air temperature. Generally, radiators are arranged against the wall under the external window. The thermal insulation of windows is insufficient compared to other envelopes, and more heat is lost through the window [6]. In addition, cold radiation caused by the window brings a certain degree of discomfort to occupants. The air adjacent to the radiator is heated and rises. When it flows through the exterior wall, heat is transferred from the air to the wall. Some heat is then lost from the exterior wall. A part of the heated air flow to the inner of the room due to the insufficient thermal buoyancy and exchange heat with the other air and surfaces of the room. Therefore, the thermodynamic state of the air near the radiator directly affects the heat transfer process among the air and surfaces in the room and the discomfort brought by the cold window

51 radiation. Precise estimation of the thermodynamic state of the airflow over the heating unit in a

52 room is of great significance for better understanding the thermal characteristics of an indoor

53 heating system [7][8][9].

54   To evaluate the thermodynamic state of the airflow over a heating unit, accurate measurement

55 is necessary. The current air temperature measurements are mainly conducted using the resistance

56 of thermal detectors (RTDs) or thermocouples. The air temperature measurement can be easily

57 performed owing to the high frequency, short response time and the ability to store large amount

58 of data of the temperature sampling instruments. On the other side, the velocity measurement

59 methods are mainly divided into two kinds: the point-wise and the globe-wise measurement

60 methods [10]. The point-wise measurement method can only reflect the velocity of the

61 representable points instead of the spatial distribution, and the measured data of measurement

62 points is mostly used as validation or boundary condition of numerical simulation. The globe-wise

63 measurement method can visualize the flow field [11]. Particle image velocimetry (PIV) is a

64 typical and the most widely used flow visualization method. The adjustment of laser and, camera,

65 tracer particle concentration, and image processing all require certain expert knowledge [12].

66 Moreover, PIV measurement system components are complex and fragile, and thus not suitable for

67 movement; therefore, this method is mostly used in laboratory research. Except some special cases

68 [13][14], traditional velocity measurement methods are rarely applied successfully in the flow

69 field measurement near the indoor heated surface. Besides the complexity of the indoor

70 environment, one of the main reasons for this is the limitation of various velocity measurement

71 technologies, which are explained in detail in [15].

72   The contradiction between the limitations of existing point-wise or globe-wise measurement

3

73   methods and the need to measure specific surface velocity has been increasing, and researchers are

74   now seeking other velocity measurement methods. The interaction of surface turbulent structures

75   with surface temperature fluctuations has been draw attention gradually. The turbulent structures

76   sweep the interface and give rise to surface temperature fluctuations [16][17]. Recent studies have

77   revealed that the characteristic of the near-surface airflow can be indirectly deduced based on

78   surface high frequency temperature fluctuations. In terms of the acquisition of high frequency

79   temperature fluctuations, thermal infrared camera is more advantageous owing to its high

80   sensitivity, short response time, and spatial resolved capability, in comparison with thermocouple

81   or resistance temperature detectors [18]. As a result, infrared thermography is gradually used as an

82   alternative tool for evaluating near-surface flow distributions. In the current study, the use of

83   infrared thermography in obtaining the characteristic of the near-surface airflow is mainly based

84   on three methods. a) Theoretically establishing the correlation between near-surface velocity and

85   temperature fluctuations based on the surface renewal (SR) theory [16]. The near-surface flow

86   structures are composed of eddies with various sizes that fluctuate with various frequencies and

87   continuously eject and sweep back to the surface. As continuously interacting with the interface,

88   the near-wall flow structures leave traces in the form of surface temperature fluctuations. In

89   addition, the near-surface eddies are distributed according to specific distribution laws [19]. By

90   exacting the eddy distribution parameters from the high frequency surface temperature

91   fluctuations, in combination with the relation between the surface velocity and near-wall heat

92   transfer, the near surface velocity can be deduced [19]. b) The other one is noted as TIV (thermal

93   image velocimetry). This method is similar to the PIV method, which estimates the near-surface

94   velocity by analyzing the displacements of the surface thermal spots within consecutive frames

4

95   captured by the infrared thermal camera. The basic principal and preliminary application of this

96   method can be referred in [15]. c) The last method is also based on the surface renewal theory.

97   Unlike the first method, the near-surface turbulent state is deduced according to the correlation

98   between the surface temperature fluctuations and the intermittent near-surface eddies and no

99   quantitative velocity is acquired.

100   **Table. 1.** Application of infrared thermography in near-surface velocity measurement

Object	Indoor/Outdoor	Scale model/ Field	Methods	Velocity Range	Reference
Horizontal plate	Indoor	Scale model	(a)	0.6－4 m/s	[19]
Evaporation plate	Indoor	Scale model	(a)	0－0.5m/s	[20]
Vertical plate	Indoor	Scale model	(b)	0－0.3 m/s	[15]
River	Outdoor	Field	(b)	0.9－1.1m/s	[21]
Volcano	Outdoor	Field	(b)	——	[22]
Solar tower	Outdoor	Field	(b)	——	[23]
River	Outdoor	Field	(b)	0－4m/s	[24]
Wall	Outdoor	Field	(b)	0－2m/s	[25]
Horizontal plate	Outdoor	Scale model	(b)	0－0.005m/s	[26]
Lava	Outdoor	Field	(b)	0－0.006m/s	[27]
Artificial turf ground	Outdoor	Field	(c)	——	[28]
Vineyard	Outdoor	Field	(c)	——	[29]
Ground	Outdoor	Field	(c)	——	[30]

101   1. (a), (b) and (c) denote the three methods described above.

102   2. Scale model and field denote the scale model experiment and the field measurement

103   Table. 1 summarizes the current main applications of infrared thermography in near-surface

104   velocity measurement. The first method obtains the near-surface spatial-averaged velocity. For

105   some specific situations, especially the flow field above the heat source, the spatial-averaged flow

106   velocity cannot reflect the spatial distribution characteristics of velocity, and thus the application

107   of this method is limited. The third method can only provide the qualitative velocity and is not

108   suitable for the evaluation of velocity distribution. Compared with the other two methods, the

109   second method can acquire the near-wall two-dimensional velocity distribution and is the most

110   widely used. As shown in Table. 1, TIV is mostly used in outdoor research at present. For both the

111   indoor and outdoor environment, the primary condition for applying TIV is that the target surface

112   should guarantee certain temperature fluctuations. In outdoor studies, especially for targets such as

113   lava or solar tower, the temperature fluctuation is intense, which is conducive to the application of

114   TIV. Nevertheless, there are still some conditions that cannot meet the temperature fluctuation

115   requirement. In some outdoor studies [25], a blackened polystyrene board was pasted on the

116   observed surface when the target surface temperature fluctuation was small. The heat capacity of

117   the polystyrene board is small and the blackened surface absorbs more solar energy. Through

118   using this method, the surface temperature fluctuations increase greatly. Compared with the

119   outdoor applications, the utilization of TIV in indoor research is more difficult because of the

120   small temperature fluctuations that occur in indoor environments. In the micro-environment over

121   the heating unit, the air near the heating unit is heated and rises vertically under the buoyancy

122   force. In addition, the vertical wall near the heating unit is generally colder than the heated air, and

123   heat is transferred from air to the wall [3]. Owing to the combined effect of the vertical cold wall

124   and the heating unit, the unique thermodynamic state of the airflow is formed. If the black-painted

125   benzene board is placed on the cold wall, it will inevitably affect the original heat transfer process,

126   and make the result deviate from the actual flow to some extent. In addition, most velocity

127   information obtained in the references summarized in Table. 1 is not validated by the other kinds

128   of mature measurement methods, and the precision of the results measured by TIV cannot be

129   guaranteed. Therefore, TIV is in its early stages of development, and its considerable potential is

130   unexplored.

131   In our earlier work, we proposed a TIV-based method for indoor environments and verified

132   the feasibility of the method for velocity measurement under natural convection [15]. However,

133   the thermodynamic state of the airflow over the heating unit and the relationship between the

134   thermodynamic state of the airflow and heating temperature and ventilation condition has not been

135   extensively explored yet. This is a subsequent study of [15] and the following questions are

136   explored:

137   1. The performance of TIV under natural convection and mixed convection.

138   2. The characteristic of the thermodynamic state of the airflow near the heating unit when the

139   heating temperature changes or mechanical ventilation is imposed.

140   **2. Methodology**

141   **2.1. Experimental setup and procedure**

142   Experiments were performed in a closed rectangular cavity shown in Fig. 1. The coordinate

143   axes are shown in Fig. 1. The cavity was placed in an air-conditioned room whose temperature

144   was maintained at 20 - 21 °C. The cavity had an internal dimension of 1200 (L) × 500 (W) × 1400

145   (H) mm. The walls were made of transparent Plexiglas. The emissivity of the cavity surfaces was

146   estimated using the infrared thermal camera and a calibrated thermocouple, and was equal to 0.90.

147   An electric heating unit of which the dimension was 500 (W) × 400 (H) mm, was attached to the

148   lower part of the vertical wall as a vertical heating element. A 5 - mm - thick polyvinyl chloride

149   with a thermal conductivity of 0.2 W/ (m·K), was stuck between the heating unit and the vertical

150   wall to decrease heat conduction from the heating unit to the back of the vertical wall. The cavity

151   was connected to the air duct, and a fan provided mechanical ventilation from the ventilation inlet

152   positioned at the bottom of the cavity. The size of the ventilation inlet and outlet was 500 (W) × 20

153   (H) mm. The heating unit was under the control of an electronic thermostat. The experimental

154 cases, shown in Table. 2, were set by adjusting the heating temperature of the heating unit and the

155 ventilation velocity.

156   Before the temperature and velocity measurements can be taken, it takes six hours in advance

157 to reach a steady state for temperature and flow fields. As shown in Fig. 1, one RTD mounted at

158 the ventilation outlet was used to measure the air temperature continuously. Once the sampled

159 temperature stabilized and the temperature fluctuation was less than 0.1 °C /min [31], it was

160 assumed that a stable thermodynamic state within the cavity has been reached, and the

161 measurements were taken.

162

Table. 2. Experimental cases

	Surface temperature of heating unit (°C)	Ventilation velocity (m/s)	Heat transfer form
Case 1	45	0	Natural convection
Case 2	65	0	Natural convection
Case 3	65	1.75	Mixed convection

163

164

165   **Fig. 1.** Experimental setup: 1. Inlet 2. Heating unit 3. CCD camera 4. Laser 5. Visualized surface

6. Outlet 7. RTD 8. Shooting positions 9. Infrared camera 10. Fan

167   **2.2 Measurements and data processing**

168   2.2.1 PIV measurement

169   As shown in Fig. 1, PIV was used to visualize the two-dimensional airflow fields that are

170   8mm and 15mm away from the vertical surface behind the heating unit. The entire visualized area,

171   which is the region above the heating unit shown as Fig. 1, is 500 (W) × 800 (H) mm. As shown as

172   Fig. 2 (a), the dimension of the view field is 280 (W) × 280 mm (H) and there are overlap areas

173   conductive to connecting the separate measurement domains. The six airflow fields are connected

174   using the technique stated in [32]. The relevant parameters of PIV system are shown in Table. 3.
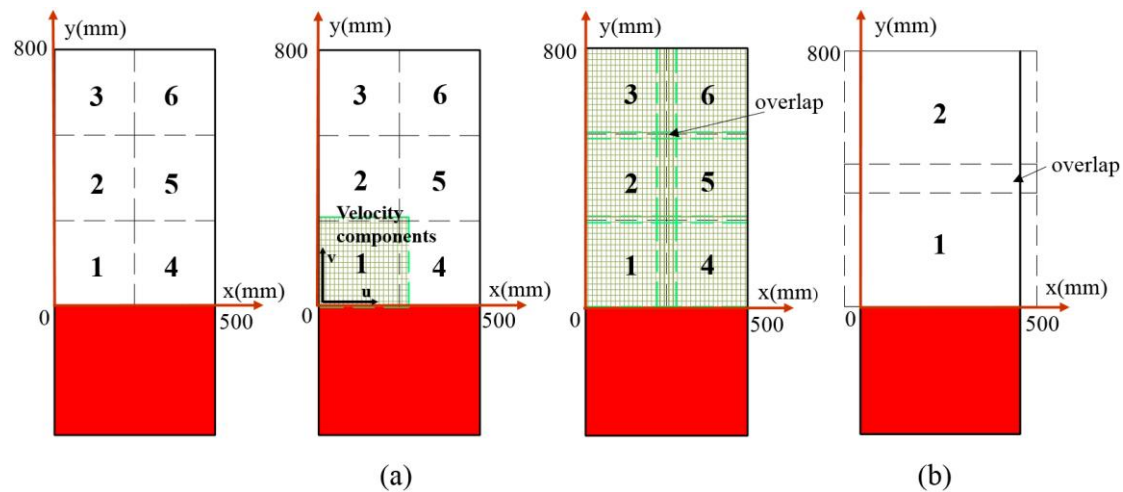
175   (a)   (b)
176   **Fig. 2.** Schematic of measurement domains a. PIV b. TIV
177   **Table. 3.** PIV parameters

Name	Parameters
Laser model and power	Double-pulsed Nd:YAG laser, 150mJ/pulse
CCD model	PIVCAM13-8
Lens model	AF Nikko 50mm f/1.8D Lens
Visual field of CCD	2048pixel × 2048pixel
Size of the interrogation window	32pixel × 32pixel, 50% overlap
Dimension of the view field	280 (W) × 280 (H) mm
Spatial resolution	0.137mm/pixel
Sampling frequency	7Hz
Sampling pairs	600

Smoke generator	VZ09−0751

178 2.2.2 TIV measurement

179   The accuracy of the measurement results cannot be guaranteed when the infrared camera

180 captures the temperature fluctuations of the target surface through the Plexi-glass. In addition, the

181 tracer particles suspended in space generate a considerable amount of scattering interference.

182 Considering these two factors, the CCD camera and the infrared camera were positioned at the

183 opposite sides. In this way, the measurement results of TIV are mirrored to make comparison with

184 the results of PIV. In each shooting position, a circle hole fit for the camera lens was dug. The two

185 holes were covered with lids to prevent the inner air from escaping. When conducting the TIV

186 measurement, the lid was removed and the infrared camera captures the surface temperature of the

187 observed Plexi-glass surface without the obstacles of any surfaces. The tiny space between the

188 camera lens and the circle hole is sealed with cotton felt to stop the air leakage. Because the

189 camera was placed and removed in a very short time and the shooting hole is very small, the

190 amount of the gas entering or exiting the cavity at the moment of removal or resetting the lid can

191 be negligible.

192   The surface temperature of the vertical wall was captured by a FLIR-T1040 infrared camera.

193 Two *.ats* video files were acquired in two shooting positions located at 600 mm and 950 mm away

194 from the bottom of the cavity. The entire visualized area is 500 (W) × 800 (H) mm and

195 decomposed into two domains and each domain area is 598 (W) × 445 (H) mm, shown as Fig.2

196 (b). The two airflow fields were connected with the method used in PIV. The detailed information

197 of the parameters for thermal image velocimetry is shown as Table. 4.

198   **Table. 4.** Infrared camera parameters

10

Name	Parameters
Model	FLIR T1040
Resolution	1024pixel $\times$ 768pixel
Sensitive wave length range	7.5~14μm
noise-equivalent temperature difference	25mK
Angel of version	28° $\times$ 21°
Dimension of the view field	598 (W) $\times$ 445 (H) mm
Spatial resolution	0.584mm/pixel
Sampling frequency	30Hz
Sampling duration	20s

199   2.2.3 Temperature measurement

200   The temperature measurement was carried out using 32 RTDs. As placing so many RTDs in

201   the cavity may disturb airflow field, the temperature measurements and velocity measurements

202   were carried out separately. The RTDs were calibrated by using a set of temperature calibration

203   system. The RTDs were calibrated in the temperature range of 18 to 46 °C, at fifteen points with

204   an interval of 2 °C. The linear calibration coefficients of the RTDs were acquired by regression

205   analysis. The maximum error of the 33 RTDs was 0.347 °C before calibration. According to the

206   linear correction of each RTD, the maximum error was decreased to 0.123 °C. The temperature

207   measurement consists of two aspects. One is to investigate the temperature distributions inside the

208   cavity, shown as the dotted square labeled "1" in Fig. 3. The other aspect is to evaluate the inner

209   heat transfer of the vertical wall and the measurement points are shown in the dotted square

210   labeled "2" in Fig. 3.
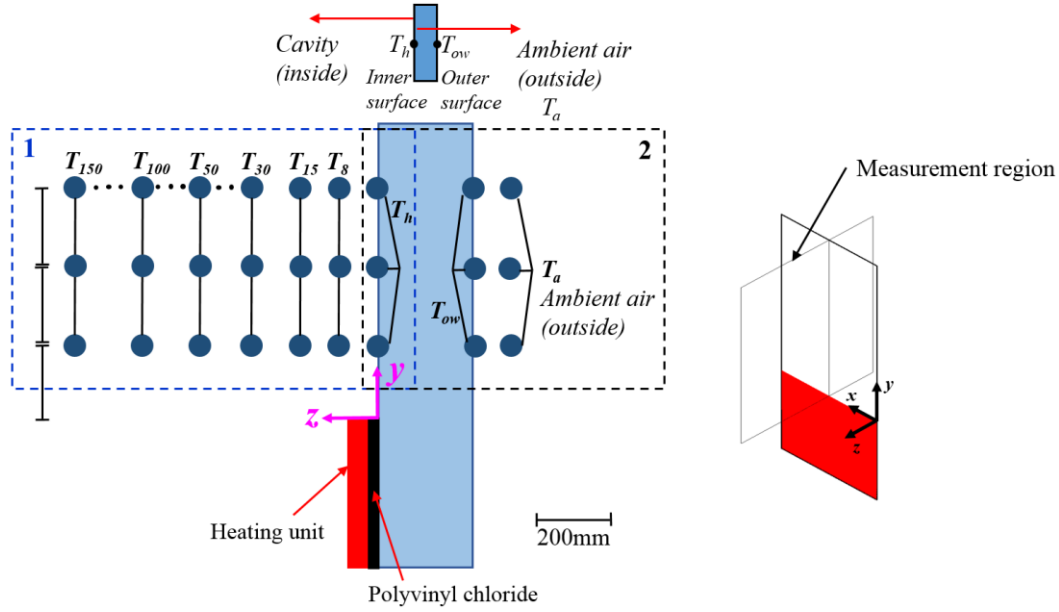
Fig. 3. Schematic distributions of temperature measurement points of the cavity

The heat transfer from the vertical wall can be obtained by the heat loss to the outside of the

cavity according to the energy balance of the vertical wall [33][34][35]. The calculation of heat

flux is based on stable conditions and the detailed calculation is as follows:

$$q_h = \frac{T_h - T_a}{A_w R_o} \tag{1}$$

Where T_h (K) is the temperature of inner vertical wall surface; T_a (K) is the temperature of the air

adjacent to the outer wall surface; and A_w (m^2), R_o (K·W^{-1}) are the area of the vertical surface and

the thermal resistance between the inner surface and the outer ambient air respectively. R_o can be

measured as:

$$R_o = \frac{1}{(h_{o,rad} + h_{o,con})A_o} + \frac{L_w}{\lambda_w A_w} \tag{2}$$

where A_o (m^2) is the area of the vertical wall that involves in heat exchange outside the cavity; λ_w

(W·m^{-1}·K^{-1}) and L_w (m) are the thermal conductivity and the height of the vertical surface; and

$h_{o,rad}$ (W·m^{-2}·K^{-1}), $h_{o,con}$ (W·m^{-2}·K^{-1}) are the radiant and convection heat transfer coefficient of the

223   outer vertical wall surface. Since the area of the outer wall surface is small enough with respect to

224   the inner surface area of the entire air-conditioned room, the radiation heat transfer coefficient of

225   the outer vertical wall surface can be calculated as:

$$h_{o,rad} = \frac{\sigma \varepsilon_o (T_{ow}{}^4 - T_c{}^4)}{(T_{ow} - T_c)} \tag{3}$$

226   where σ (W·m^{-2}·K^{-4}) is the Stefan-Boltzmann constant, ε_o is the surface emissivity of the outer

227   wall surface and is equal to 0.90, T_{ow} (K) and T_c (K) are the temperature of outer vertical wall

228   surface and the inner surface of the air-conditioned room.

229   The convection heat transfer coefficient can be manipulated as:

$$h_{o,\mathrm{con}} = \frac{Nu\lambda_w}{H_w} \tag{4}$$

230   where H_w (m) is the height of the vertical wall that involves in heat exchange outside the cavity,

231   Nu is the dimensionless parameter which is calculated using the correlation summarized in [36]

232   based on the Rayleigh number.

233   The distributions of temperature points are shown as Fig. 3. Twenty-one RTDs were inserted

234   at the following locations: x = 250 mm as shown as Fig.1, at heights of 200 mm, 400 mm, 600

235   mm away from the upper level of the heating unit along y axis, and at 0 mm, 8 mm, 15 mm, 30

236   mm, 50 mm, 100 mm, 150 mm away from the vertical wall along the z axis. Six RTDs were

237   mounted at x = 250 mm and at heights (y direction) of 200 mm, 400 mm, and 600 mm; they were

238   used to capture the outer vertical wall surface temperature and the temperature of the air adjacent

239   to the outer surface. Four RTDs were used to measure the inner wall surface temperature of the

240   air-conditioned room, and the temperature of the air-conditioned room was obtained by one RTD
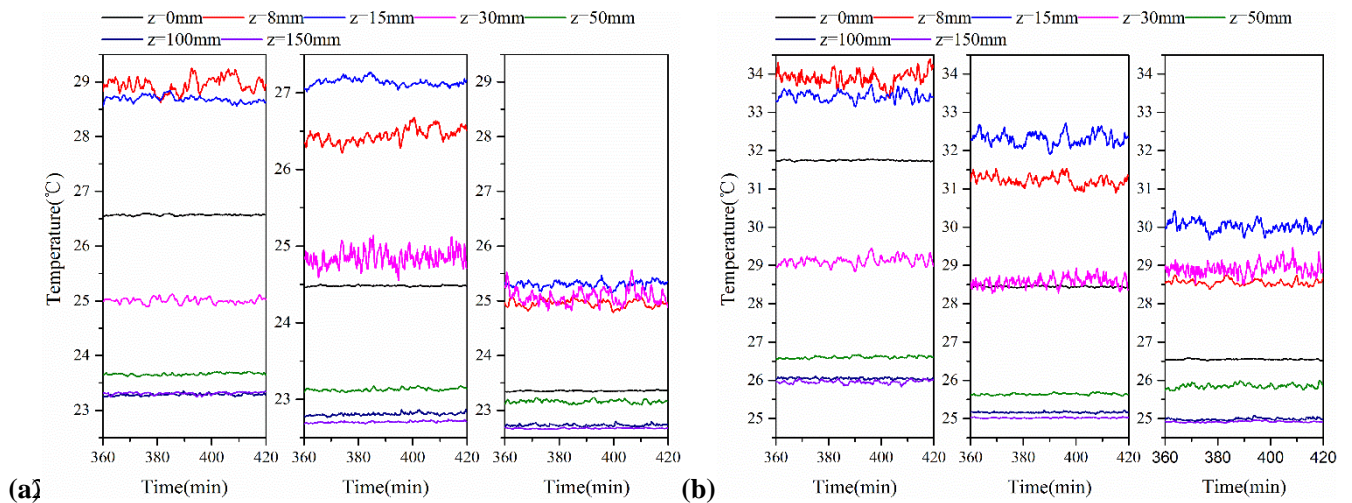
241   placed in the center of the room. The temperature series were stored in a computer by using the

242   Agilent 34980A multiplexer module. The sampling frequency was 0.1 Hz, with a response time of
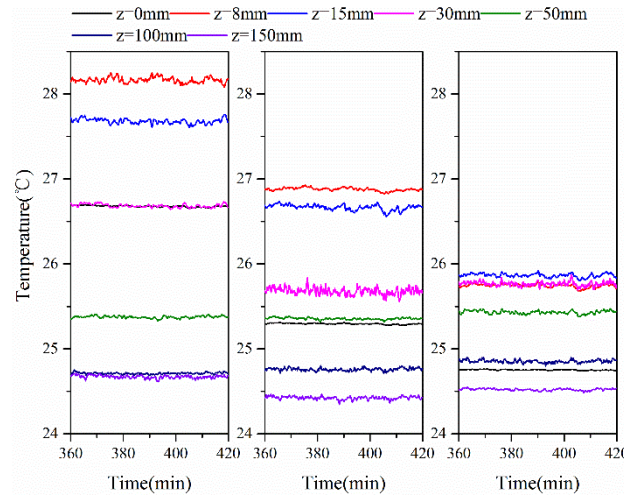
243   10 s.

244   **3. Results**

245   **3.1. Evaluation of temperature measurements**

246   3.1.1 Temperature distributions

247   Fig. 4 (a) - (c) show the temperature series of three cases in continuous time during the last

248   one hour. In Fig. 4 (a), (b), (c), the three subfigures from left to right represent the temperature

249   series at the heights of 200 mm, 400 mm and 600 mm. The temperature fluctuation near the

250   vertical surface is large at positons within 30 mm from the vertical wall. When the distance is

251   larger than 30 mm, the temperature tends to be relatively stable. As the heating temperature

252   increases, the air temperature near the vertical surface and the temperature fluctuation increases.

253   When mechanical ventilation is imposed, the near-wall air temperature and the temperature

254   fluctuation decreases.

(a)   (b)

The legend at top reads: z=0mm, z=8mm, z=15mm, z=30mm, z=50mm, z=100mm, z=150mm

256 **(c)**

257 **Fig. 4.** Temperature series of the *y*- positions, 200mm, 400mm, 600mm of the three cases (a) *Case*

258 *1* (b) *Case 2* (c) *Case 3*

259 The distributions of the time-averaged air temperature in the three cases presented in Fig. 5

260 show a similar distribution trend, which is an increase to a peak value and a gradual decrease. The

261 temperature of the heating unit and the ventilation condition not only affect the temperature

262 magnitude in the cavity, but also the temperature distribution characteristics. With an increase in

263 heating temperature, the air temperature in space increases significantly. The gradient of the air

264 temperature near the vertical surface increases dramatically as well. Under the effect of

265 mechanical ventilation, the air temperature of Case 3 tends to be more uniform, and the

266 temperature gradient near the vertical wall is largely weakened and approaches that of condition of

267 Case 1, even though the heating temperature is higher.

268 As stated in [3][15], due to the insufficiency of the thermal buoyancy driving force, part of

269 the hot airflow above the heat source deviates from the original flow direction. Due to flow

270 detachment, the air temperature distribution also exhibits the same detachment [3]. The hot air

271 flows upward for some distance until the buoyancy force is smaller than gravity and rushes to the

272 inner regions of the cavity. At the height of 200 mm for all the cases, the air temperature increases

273 to a maximum value in the plane that is 8mm away from the vertical surface and then keeps

15

274 decreasing. If no temperature detachment exists, the trends at the other heights should also follow

275 the same law as that at the height of 200 mm. However, in Case 1 and Case 2, the maximum air

276 temperature occurs 15 mm away from the vertical surface at heights of 400 mm and 600 mm. In

277 consequence, there exists a temperature detachment. In Case 3, there also exists a temperature

278 detachment according to the changing tendency. Unlike the other natural cases, the maximum

279 temperature occurs in 8mm away from the vertical surface at the heights of 200 mm and 400 mm.

280 For the height of 600 mm, the maximum air temperature occurs 15mm away from the vertical wall.

281 The temperature detachment height rises to 600 mm under the effect of mechanical ventilation.

282
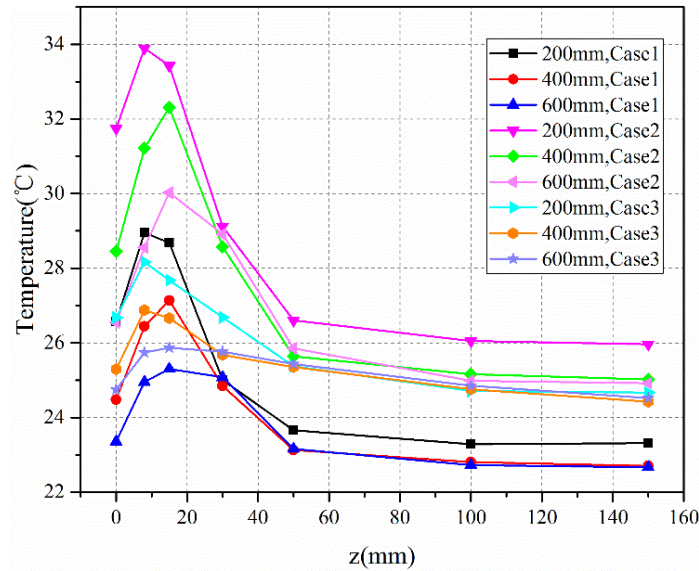
283 **Fig. 5.** The distribution of time-averaged temperature of three cases.

284 3.1.2 Heat transfer of the inner vertical wall

285   Based on the data processing method mentioned earlier, the inner heat transfer of the vertical

286 wall was calculated and is shown in Fig. 6. Similar to the trend of the inner surface temperature,

287 the heat flux of all the cases decreases with an increase in height. As the heating temperature

288 increases, the inner surface temperature of the vertical wall increases, and the potential difference

289 between the inner wall and the air outside the cavity increases; therefore, the heat loss to the outer

16

290   wall increases. Although the surface temperature of the heating unit in Case 3 is identical to that in

291   Case 2, the heat flux of the inner wall is much smaller than that of Case 2.
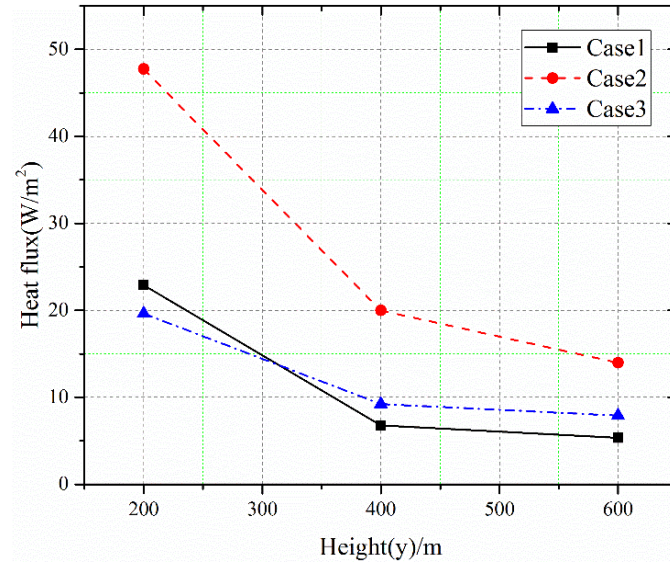
292
293   **Fig. 6.** The heat transfer of inner vertical wall

294   The energy balance of the vertical wall influences the heat transfer rate significantly. The

295   schematic heat balance of the vertical wall is shown as Fig. 7(a). In steady state, the heat storage

296   of the vertical wall is not taken into accountant. For the inner surface of the vertical wall, the heat

297   transfer process includes the radiative and convective heat transfer in the cavity and the heat loss

298   to the air adjacent to the outer wall. The radiative heat transfer rate of the inner wall is calculated

299   by establishing the radiative heat transfer network [37]. The other five inner surfaces are viewed as

300   a single surface since the temperature difference between each wall surface is not significant. The

301   single surface, the heating unit and the vertical wall constitute a closed radiation heat transfer

302   system. The surface thermal resistance is calculated by $R_i = (1-\varepsilon_i)/(A_i\varepsilon_i)$, where ε is the surface

303   emissivity, $A_i (\mathrm{m}^2)$ is the surface area. The space thermal resistance is calculated by $R_{ij} = 1/(A_i X_{ij})$,

304   where X_{ij} is the view factor from surface i to surface j. Since the vertical wall and the heating unit

305   are arranged in parallel, the view factor between the two surfaces is 0. According to heat balance,

306 the convective heat transfer rate is the sum of the heat loss and the radiative heat transfer rate. The

307 heat transfer rates of the three cases are shown are Fig. 7 (b)-(d). As shown in Fig.7, compared

308 with the radiative heat transfer, the convective heat transfer occupies a large proportion and has a

309 decisive role in the net heat flux of the vertical wall.
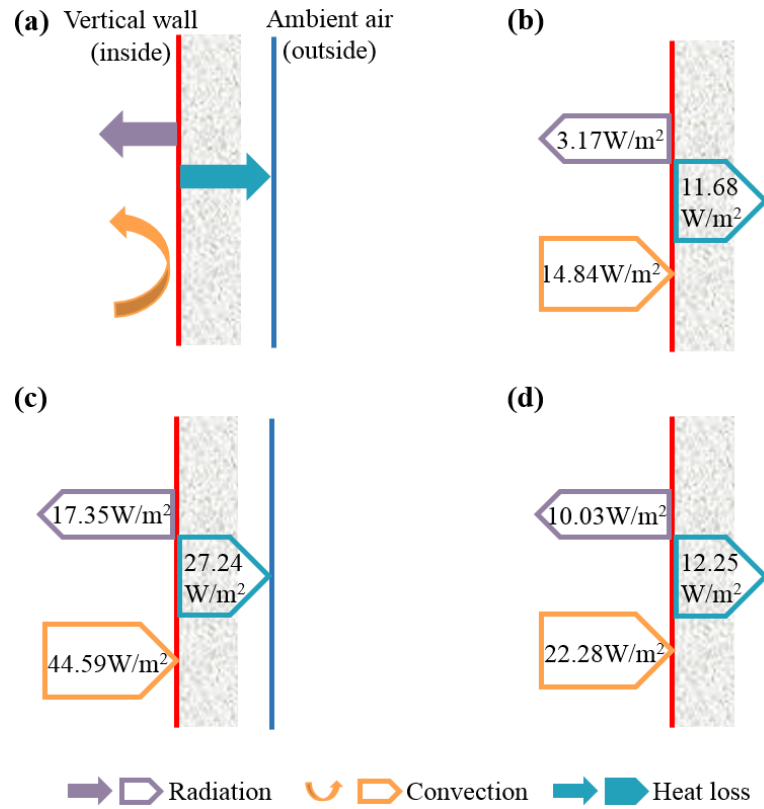
310

311 **Fig. 7.** (a) Schematic heat balance of the vertical wall, (b)-(d) detailed heat transfer rates of *Case 1*
312 to *Case 3*.

313 In the convective heat transfer process, the air flow rate affects the heat flux. Here, an

314 evaluation of the air flow rate based on the PIV measurement results was made. In the thin layer

315 near the wall, heat transfer occurs between the air and the wall and thus the air flow rate used to

316 calculate the heat flux should be close to the wall. We used the velocities in the plane that is 8mm

317 away from the vertical wall to calculate the air flow rate. The velocities in the 8mm plane are

318 averaged and the spatial-averaged velocities of Case 1 to Case 3 are 0.22m/s, 0.27m/s, and

319 0.96m/s. The air flow rates of Case 1 and Case 2 are shown to be smaller than that of Case 3.

320   Therefore, in this study, the impact of the air flow rate is not significant compared with the other

321   influencing factors.

322   The thickness of the thermal boundary layer is an essential factor to evaluate heat transfer.

323   With the increase of heating temperature, the heat transfer efficiency is enhanced, and the thermal

324   boundary layer of Case 2 should be thinner than that of Case 1. As a result, through comparing the

325   thickness of the thermal boundary layer of Case 2 and Case 3, the relative heat transfer efficiency

326   of natural convection and the mixed convection can be determined. In this study, the thickness of

327   the thermal boundary layer of Case 2 and Case 3 in the height of 200mm was compared. The

328   Rayleigh number Ra ($= g\beta(T_s - T_\infty)L^3 \Pr/\upsilon^2$) and the Reynolds number Re ($= UL\upsilon^{-1}$) of Case

329   2 and Case 3 are calculated, where β (K^{-1}) is the thermal expansion coefficient, T_s (K) is the

330   surface temperature, T_∞ (K) is the temperature of the mainstream and is regarded as the air

331   temperature in the center of the cavity, and L(m) is the reference height of the vertical wall and is

332   determined to be 0.2. Through calculation, it is found that the boundaries of the two cases are

333   laminar. For the case of isothermal vertical surface under natural convection, the thickness of the

334   thermal boundary layer can be calculated as $\delta = 5.3\left(\dfrac{g\beta(T_s - T_\infty)}{\nu^2}\right)^{-0.25} L^{0.25}$ [36]. In this study,

335   the vertical wall is non-isothermal. If T_s is taken as the temperature of the surface in the height of

336   200mm, the calculated thickness of the boundary later would be larger than the real value. In

337   consequence, T_s is taken as the average temperature of the surface in the region of 0-200mm. For

338   the case of isothermal vertical surface under mixed convection, the thickness of the thermal

339   boundary layer of the mixed convection can be calculated as $\delta = \dfrac{5L}{Re^{0.5}}$ [36]. Then the

340   thicknesses of the thermal boundary layers of Case 2 and Case 3 can be estimated to be 0.0125m

341   and 0.0066m. Therefore, the thickness of the thermal boundary layer of the natural convection

342   cases are thicker than that of the mixed convection case. The change of heat flux is not consistent

343   with the change of boundary layer, but presents an opposite trend.

344   However, as far as the experimental results in this study is concerned, the heat transfer cannot

345   be only evaluated by the thickness of boundary layer. The thickness of the boundary layer is the

346   combined effect of the flow and heat transfer. The basic factor that influencing the heat flux is the

347   thermal and flow state of the air. In order to evaluate the factors contributing to the heat flux, the

348   temperature and the velocity of the air should be inspected. In the previous response, we have

349   analyzed the influence of the velocity and air flow rate. Next, the temperature difference between

350   the near-wall air and the vertical wall is taken into accounted. Fig. 8 shows the temperature

351   difference between the vertical wall and the air 100mm away from the vertical wall. As shown in

352   Fig. 8, for Case 3, the temperature difference between the air and the vertical wall decreases

353   significantly and even lower than that of Case 1. As a result, the temperature difference between

354   the air and the vertical wall has a significant impact on the magnitude of the heat flux compared to

355   the other factors.

356
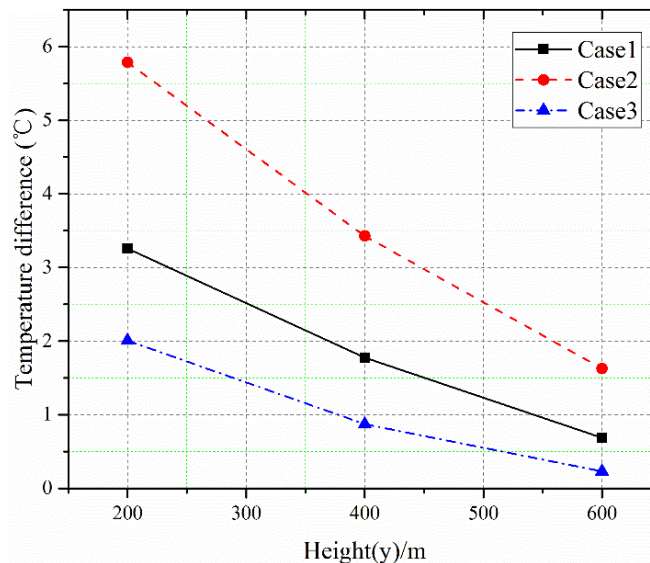
357   **Fig. 8.** The temperature difference between the vertical wall and air 100mm away from the
358   vertical wall

359   Furtherly, since the heat is transferred from the near-wall air to the vertical wall, the

360   temperature of the near-wall air is critical to the magnitude of the heat flux of the vertical wall. In

361   natural convection case, the air is heated and circulated in the cavity and no air enters in the air

362   duct. Under the effect of the fan, the near-wall air of Case 3 flows out of the cavity along the outlet

363   positioned in the top of the cavity. In this study, the air duct is not insulated and its heat

364   conductivity coefficient is evidently larger than that of the cavity. A huge amount of the heat

365   obtained in the cavity is released from the air duct to the air-conditioned room. With the

366   continuous heat release process, the inlet air temperature of Case 3 is lowered significantly. As a

367   result, the heat flux of Case 3 is similar to that of Case 1 even though the heating temperature is

368   20°C higher.

369   **3.2. Evaluation of flow structures**

370   3.2.1 Time averaged velocity distributions

371   As mentioned previously, the two-dimensional velocity of the two planes that are 8 mm and

372   15 mm away from the vertical wall were measured by PIV. For the convenience of illustration, the

373   velocities of the plane that were 8 mm and 15 mm away from the vertical wall that were measured

374   by PIV are denoted as PIV8 and PIV15, respectively. The measured results of thermal image

375   velocimetry are denoted as TIV. By averaging the instantaneous velocities, the time-averaged

376   velocity fields measured by PIV and TIV under three cases can be obtained (Fig. 9 to Fig. 11).

377   Fig. 9 shows the time-averaged velocity filed of Case 1. From the perspective of the spatial

378   distribution, the measured velocity shows vertical variation to some extent. As the height increases,

379 the velocity gradually increases and reaches at maximum value at a height of 200 mm. The

380 velocity is maintained at a high level until the height increases to 400 mm. As the height continues

381 to increase, the velocity decreases gradually due to an insufficient buoyancy force. The

382 distribution trend of Case 2 is similar to that of Case 1. However, due to an increase in heating

383 temperature, the velocity distribution exhibits a more pronounced spatial difference in the vertical

384 direction. In Case 2, the peak velocity appears at a height of 400-600 mm, which is higher than

385 that of Case 1. Correspondingly, the maximum velocity value increases as well. Different from the

386 distributions presented in Case 1 and Case 2, the velocity distributions of Case 3 show a

387 decreasing trend with an increase in height. In Case 3, natural convection and mechanical

388 ventilation have a synergistic effect on velocity distribution. As can be seen from Fig. 10, the

389 influence of mechanical ventilation is stronger than that of natural convection and the velocity

390 distribution characteristics are mainly determined by mechanical ventilation.

391   Further inspection of the relative magnitude of PIV15 and PIV8 shows that PIV15 is smaller

392 than PIV8. The plume originates from the heating unit and rises to the upper quiescent region. As

393 the perpendicular distance from the heating unit increases, the scale of the plume increases,

394 eventually dissipating in the quiescent region owing to a decrease in buoyancy force caused by the

395 cooling of cold air and viscous effects [36]. Due to an insufficient thermal buoyancy, the velocity

396 decreases with an increase in perpendicular distance. As a result, the velocity in the plane that is

397 15 mm away from the vertical wall is lower than the velocity in the plane that is 8mm away from
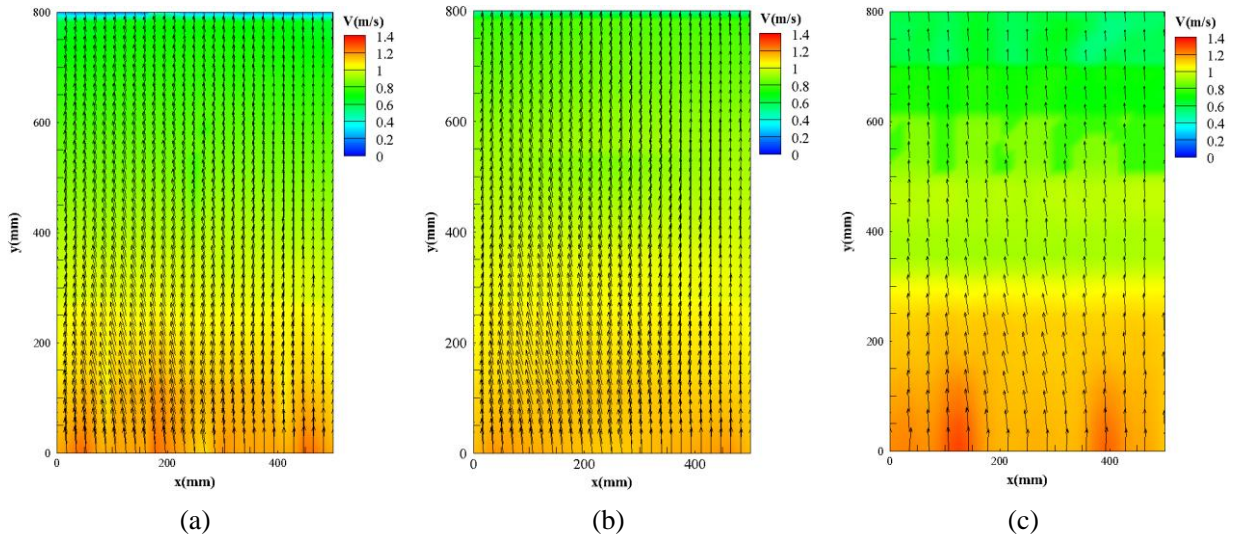
398 the vertical wall.
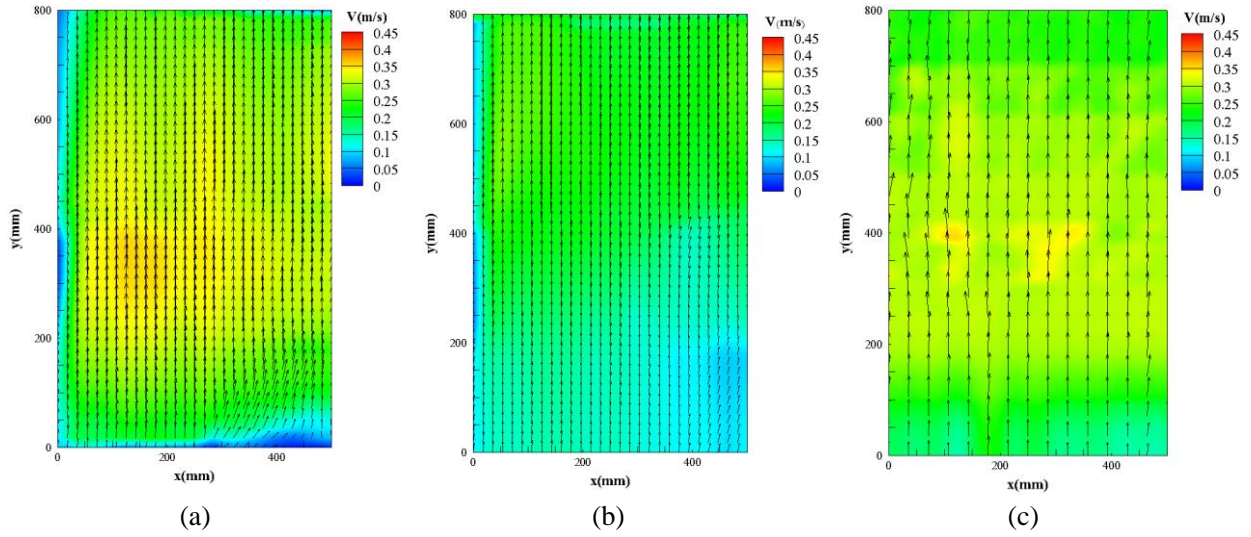
399   **Fig. 9.** Time-averaged velocity of *Case 1*, (a) PIV8, (b) PIV15, (c) TIV

400
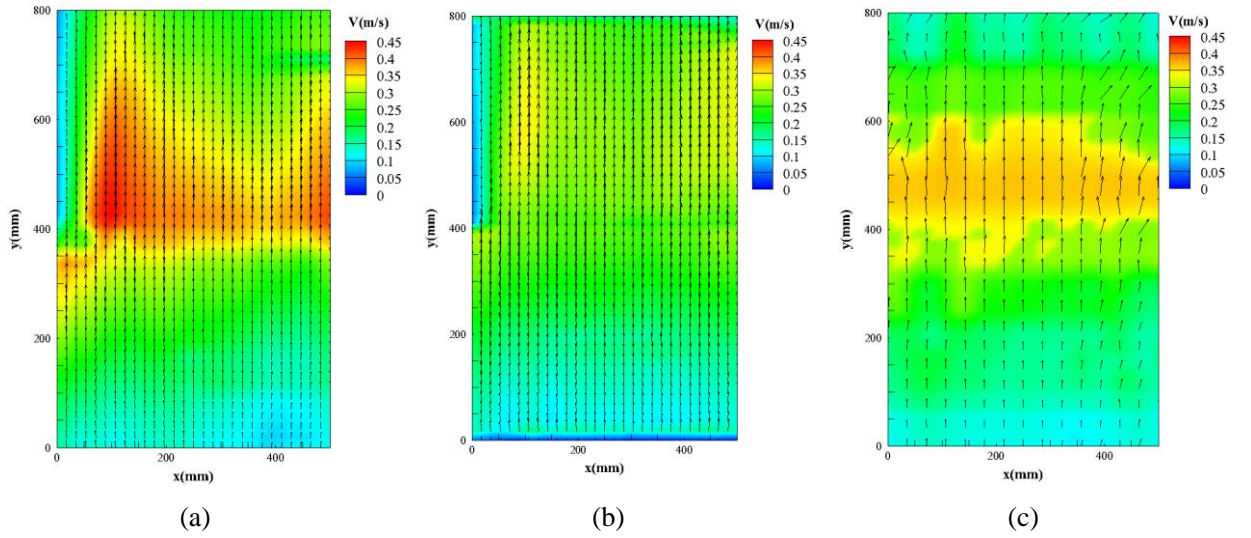
401   **Fig. 10.** Time-averaged velocity of *Case 2*, (a) PIV8, (b) PIV15, (c) TIV


402   **Fig. 11.** Time-averaged velocity of *Case 3*, (a) PIV8, (b) PIV15, (c) TIV

403   On the whole, the velocity fields measured by TIV are close to those measured by PIV,

404   especially the measurement results of PIV8. However, in the three Cases, differences between TIV

405   and PIV8 can be observed. The differences are directly related to the difference in measurement

406   method principles. In the interaction between the wall surface and flow structures, heat is

407   exchanged with the ejections and sweep of intermittent eddies. An essential factor that used to

408   evaluate the heat transfer is the thickness of the boundary layer. As the heating temperature

409   increases or mechanical ventilation is imposed, the thickness of boundary layer becomes thinner

410   and the heat transfer is more intense. In TIV, the velocity is obtained by detecting the fluctuations

411   of surface thermal spots. The temperature pattern captured by the infrared camera is closely

412   related to the boundary layer [38]. As the thickness of the boundary layer changes, the "position"

413   of the flow field measured by TIV changes accordingly. However, in the PIV experiment, the flow

414   field of the planes that are 8 mm and 15 mm away from the vertical surface were measured, and

415   thus, the measurement position is always fixed. With the change in the thickness of the boundary

416   layer, the relative positions of PIV8 and TIV changes, and thus, the measurement results of TIV

417   and PIV8 exhibit a certain difference in the three cases.

418   Overall, in natural convection and mixed convection, TIV and PIV8 are close, and both are

419   more consistent in magnitude and trend. The position where the maximum velocity occurs and the

420   magnitude of velocity can be accurately interpreted by TIV. Therefore, TIV has a certain

421   feasibility in reflecting the spatial distribution characteristics of the near-wall airflow.

422   The histograms of velocities at $x = 250$ mm and $y = 200$ mm for all the cases are shown in

423   Fig. 12. As a whole, the distributions of PIV8 and TIV are similar, which shows that the

424   statistical results are reliable. It is can be observed that, in PIV8, the large velocity values account

425   for a larger proportion than that in the TIV for the three cases. This is because that there exists a

426   lag between the surface temperature fluctuation and the near-wall velocity fluctuation. When the

427   near-wall airflow changes, the surface shows the trace of the airflow in the form of surface

428   temperature fluctuations. However, due to the heat storage of the vertical wall, the surface

429   temperature cannot change immediately when the near-wall flow changes. As a result, the surface

430   temperature fluctuations are weaker than those in the ideal situation, and the TIV measurement

431   results tend to be distributed in the low velocity range.

432   (a)

433   (b)

434   (c)
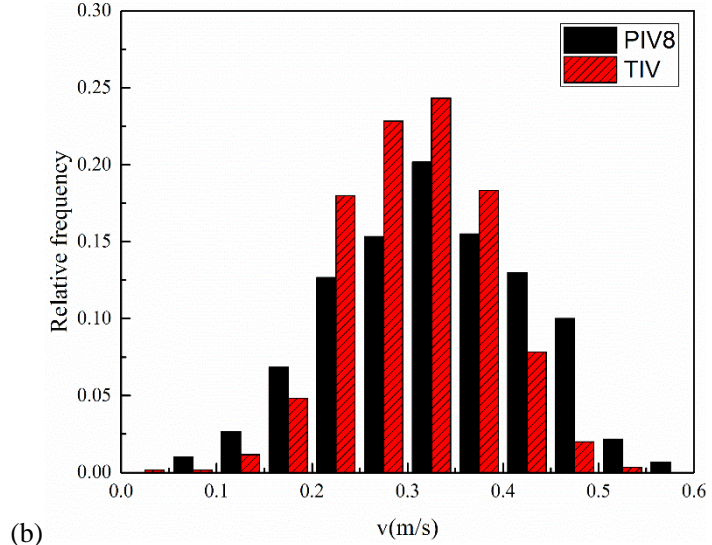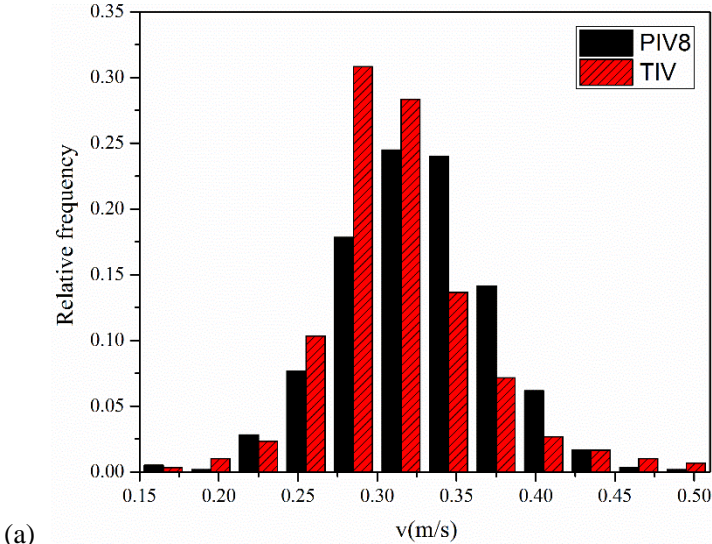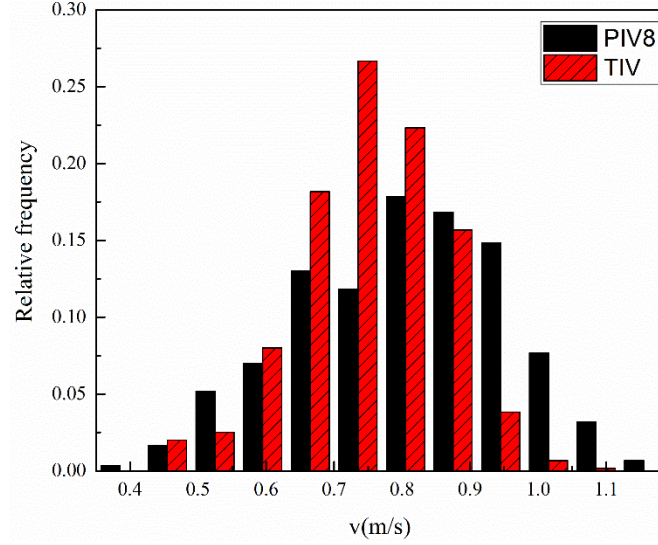
435   **Fig. 12.** The histograms of velocity at *x*=250mm, *y*=200mm, (a) *Case1*, (b) *Case 2*, (c) *Case 3*

436   3.2.2 Power spectrum analysis

437   The power spectrum analysis of the airflow fluctuation can be used to reveal the energy

438   distributions in a frequency range and characterize the turbulent airflow [39]. The fluctuating

439   velocity (v') is obtained by subtracting the instantaneous velocity from the time-averaged velocity.

440   Based on the velocity fluctuation, the power spectrum density function can be defined as follows:

$$\int_0^\infty E(f)df = \overline{v'^2} \tag{5}$$

441   where E(*f*) (m^2/s) is the power spectrum density function, *f* is the frequency (Hz).

442 (a)   (b)
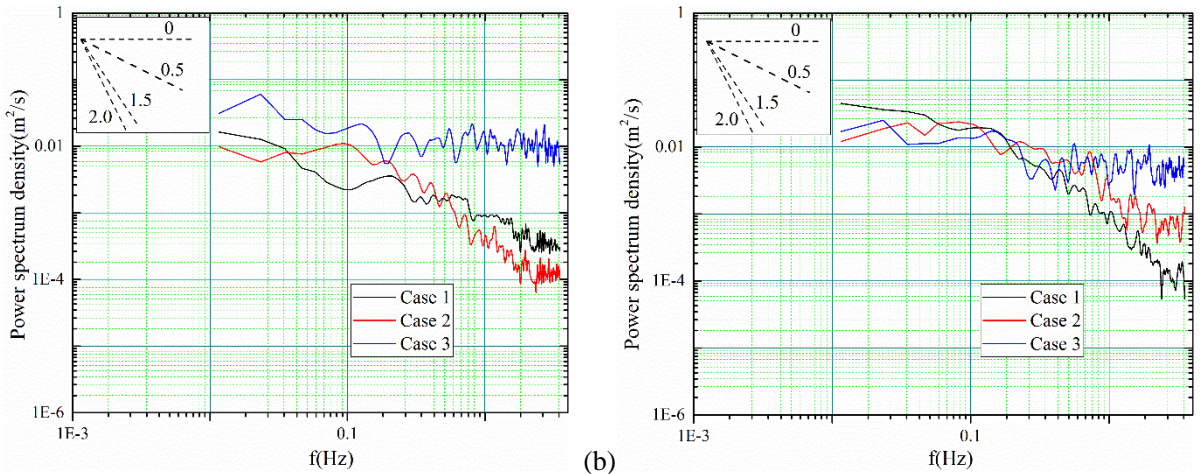
443   **Fig. 13.** Power spectra (a) at the height of 200mm; (b) at the height of 600mm

444   Fig. 13. (a) and (b) show the power spectrum density measured by PIV at the heights of 200

26

445   mm and 600 mm, respectively. The spectrum distributions of the velocity fluctuation of the three

446   cases show a similar tendency, but there are still some differences in the inertial subrange. The

447   negative slope of the logarithmic power spectrum curve of natural convection are between 1.5-2.0,

448   while the negative slope of the mixed convection case is within 0-0.5. This phenomenon was also

449   observed by [40]. The negative slope of the inertial subrange in natural convection are close to 5/3,

450   showing that the flows are fully developed. The turbulence of Case 3 differs from that in the other

451   cases, as it is influenced by the jet at the bottom of the cavity. With the diffusion of the jet airflow

452   in the cavity, the average velocity decreased slightly, and the turbulence decreased slightly

453   accordingly.

454   The pre-multiplied power spectrum is obtained by multiplying the power spectrum of

455   velocity and the wave number, which can be used to show the contribution of different wave

456   number on kinetic energy. The pre-multiplied velocity spectra at $x = 250$ mm, $y = 200$ mm of TIV

457   and PIV8 of the three cases are shown as Fig. 14.

458   (a)   (b)

459   (c)
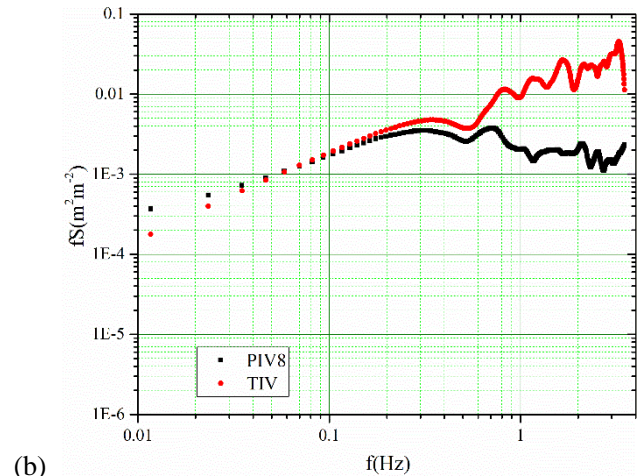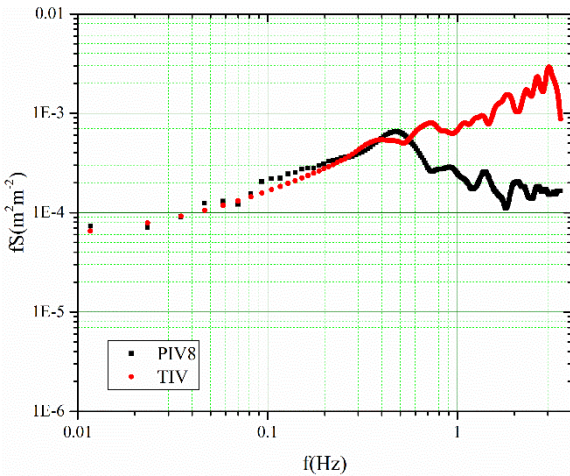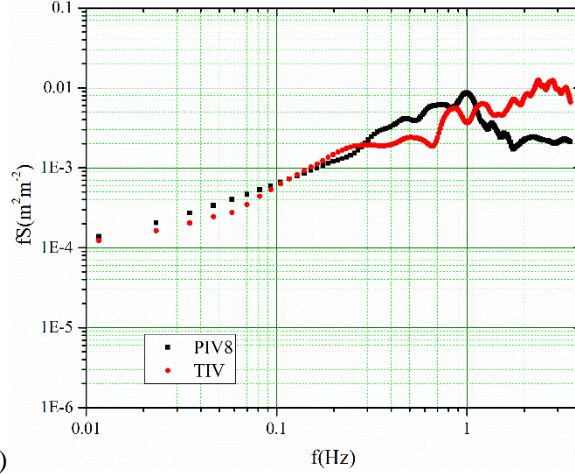
Fig. 14. Pre-multiplied power spectra of (a) *Case 1*, (b) *Case 2*, (c) *Case 3*

As can be seen from Fig. 14, the spectral shapes of the three cases all fit well in the low−frequency regions. As stated in [41], the turbulent flow consists of large scale and small scale structures. The large scale structures fluctuate with low frequency and represent the main motion of turbulent flow. The small scale structures are distributed in the high-frequency region and are advected by large scale structures. The great fitness in the low−frequency region means that the measurement results of TIV can reflect the main flow characteristics of turbulent flow motion. In the higher frequency regions, the spectral curves separate and the pre-multiplied power spectrum of TIV is more energetic than PIV, which is also observed in [25]. Due to the wall shear stresses, the closer to the wall, the more energetic the flow fluctuation is. The peak of the pre-multiplied spectra appears in the higher frequency region, which means that the airflow field evaluated by TIV may be closer to the vertical wall than the airflow field measured by PIV.

4. Discussion

In the foregoing section, we mentioned that the measurement results of TIV are influenced by the boundary layer. By analyzing the pre-multiplied spectrum of PIV and TIV, it is deduced that the position of the airflow field evaluated by TIV may be closer to the wall than the airflow field

28

476   of the fixed plane measured by PIV. Although the measurement position of TIV cannot be directly

477   determined, the dynamic characteristics of the PIV and TIV measurements provide a new

478   perspective for estimating the information of the near-wall airflow field. We attempted to

479   indirectly judge whether the result of the TIV measurement is affected by the boundary layer by

480   judging the relative position of the two airflow fields measured by PIV and TIV and the boundary

481   layer.

482   From the perspective of physical structure, turbulent flow can be regarded as a superposition

483   of vortices with various sizes. Large scale vortices fluctuate with low frequency and extract energy

484   from the mainstream. Through the interaction of vortices, energy is gradually transferred to the

485   small-scale vortices which fluctuate with high frequency. Finally, due to fluid viscosity, small

486   scale vortices disappear and the mechanical energy is converted into thermal energy of the fluid.

487   The spectrum of temperature can be calculated as follows:

$$E_\theta = \int_0^\infty E_\theta(\mathrm{k})dk \tag{6}$$

488   where E_θ is the power spectrum density function of temperature, k is the wave number.

489   The exponential slope of the region between the flat low-frequency and the sharp drop at the

490   high frequency represents the efficiency of energy transformation from the large scale to the small

491   scale structures. In Zhang' study [42], it was found that the efficiency of energy transformation

492   near the vertical surface varies greatly and reaches a maximum value near the boundary layer.

493   Outside the boundary layer, the energy transformation efficiency almost remains constant with a

494   constant exponent. As a result, it appears that the efficiency of the transformation from the large

495   scale structure to the small scale structures can be used to estimate the position of the boundary

496   layer. Based on this characteristic, we measured the temperature fluctuation of the air near the

497   vertical surface and explored the slope of the power law distribution region.

498   An appropriate temperature sampling frequency is required to obtain the real-time

499   information about the temperature field. However, due to the limitations of the measurement

500   instrument, the sampling frequency is always restricted. The Kolmogorov time scale is used to

501   evaluate whether the measurement frequency is sufficient. The Kolmogorov time scale can be

502   calculated as: $\tau = (\nu/\varepsilon)^{0.5}$, $\varepsilon = U^3/H$, where ν is the turbulent viscosity, ε is the turbulent

503   dissipation rate, U is root mean square velocity, H is the turbulence length scale. In this study, the

504   Kolmogorov time scale is 0.245 s for Case 1. The temperature fluctuations were collected by

505   Angilent 34980A with a frequency of 7 Hz. The response time is 0.143 s, which is smaller than the

506   Kolmogorov time scale for Case 1. In consequence, the data collected at 7 Hz can be used to

507   evaluate the energy transformation efficiency.
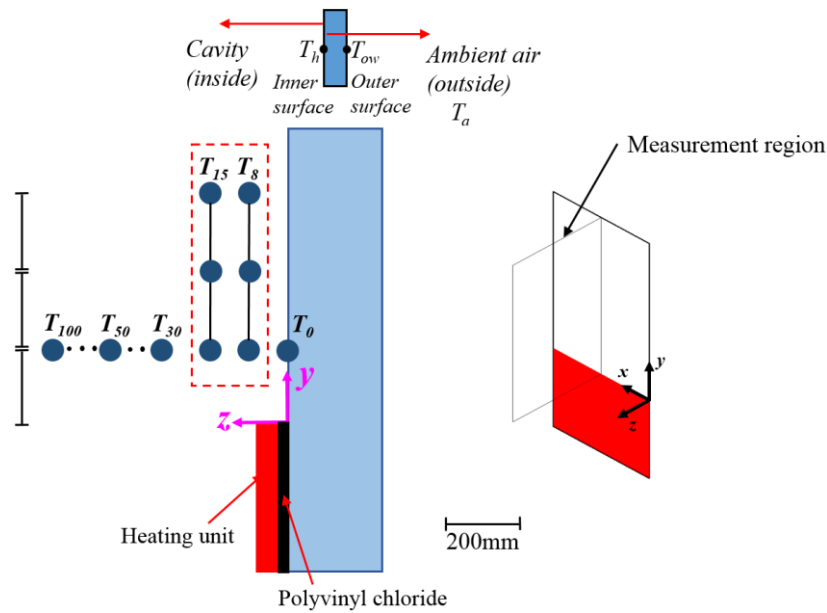

508
509   **Fig. 15.** Schematic distribution of temperature measurement points

510   As shown in Fig. 15, the temperature fluctuations of the ten points were measured. The

511   power spectrum distributions of the six points in the planes that are 8 mm and 15 mm away from

512   the vertical surface are shown in Fig. 16. The six points have the same arrangement as the former

30

513   temperature measurement arrangement. The power spectrum distributions of the other four points

514   located at the height of 200 mm, and are 0 mm, 30 mm, 50 mm, 100 mm away from the vertical

515   surface are presented in Fig. 17. The line are fitted in the power law distribution region and the

516   slopes are shown in figures.

517   For the plane that is 8 mm away from the vertical surface, energy transfer efficiency

518   decreases with an increase in height. As for the plane that is 15 mm away from the vertical surface,

519   heat transfer efficiency is almost constant and is smaller than that for the plane that is 8 mm away

520   from the vertical surface. Combining Fig. 16 and Fig. 17, it can be found that the energy

521   transformation efficiency increases from 0 mm to 8 mm. The efficiency decreases from 8 mm to

522   15 mm and remains almost constant within 15 mm to 30 mm from the vertical surface. When the

523   distance is increased to 50 mm, the efficiency decreases greatly. When distance increases and for

524   to the regions far away from the vertical surface, the efficiency reduces due to a small temperature

525   gradient and weak convection. According to the aforementioned analysis, the efficiency increased

526   to its maximum value near the boundary layer and remains almost constant outside the boundary

527   layer. It can, therefore, be deduced that the plane that is 8 mm away from the vertical surface is

528   near the boundary layer, and the plane that is 15 mm away from the vertical surface is outside the

529   boundary layer. In combination with the fact that the TIV velocity is close to that of PIV8, it can

530   be identified that the velocity plane measured by TIV is also near the boundary layer. Although

531   unable to establish a direct relation, it is ascertained that the measured results of TIV can reflect

532   the dynamic characteristics of the near-wall region in either natural or mixed convection.

533
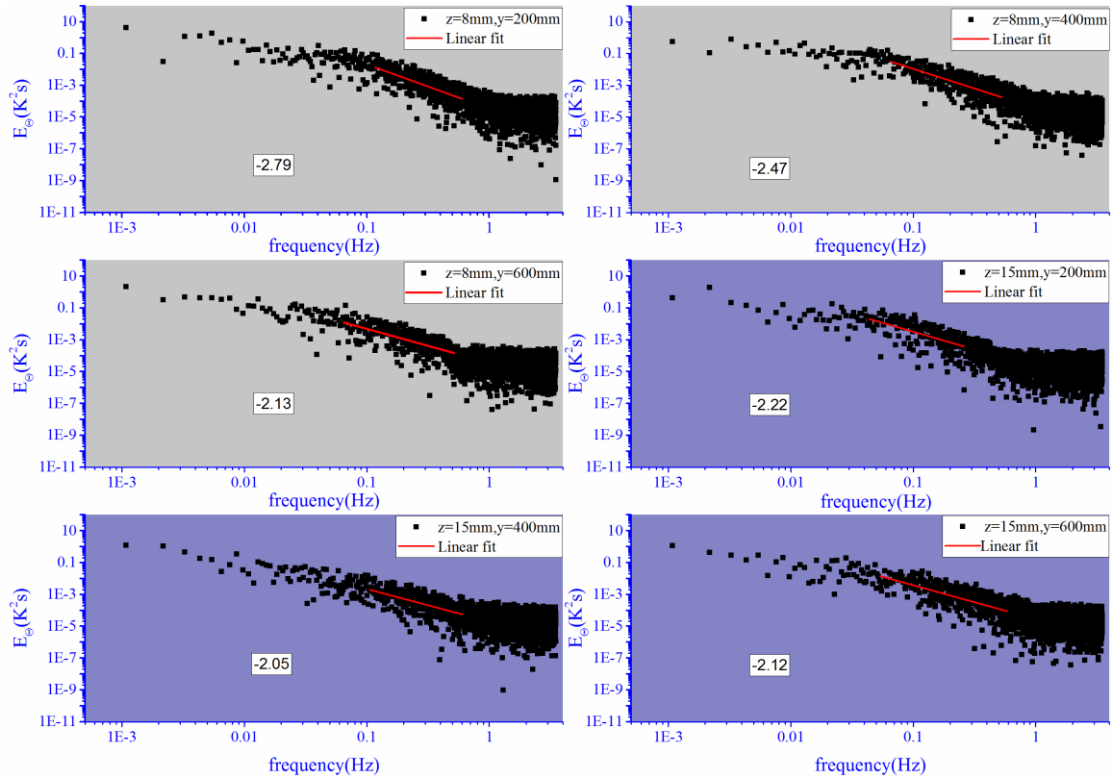
Fig. 16. Power spectrum of temperature of the points in the plane of 8mm and 15 mm away from the vertical surface

536
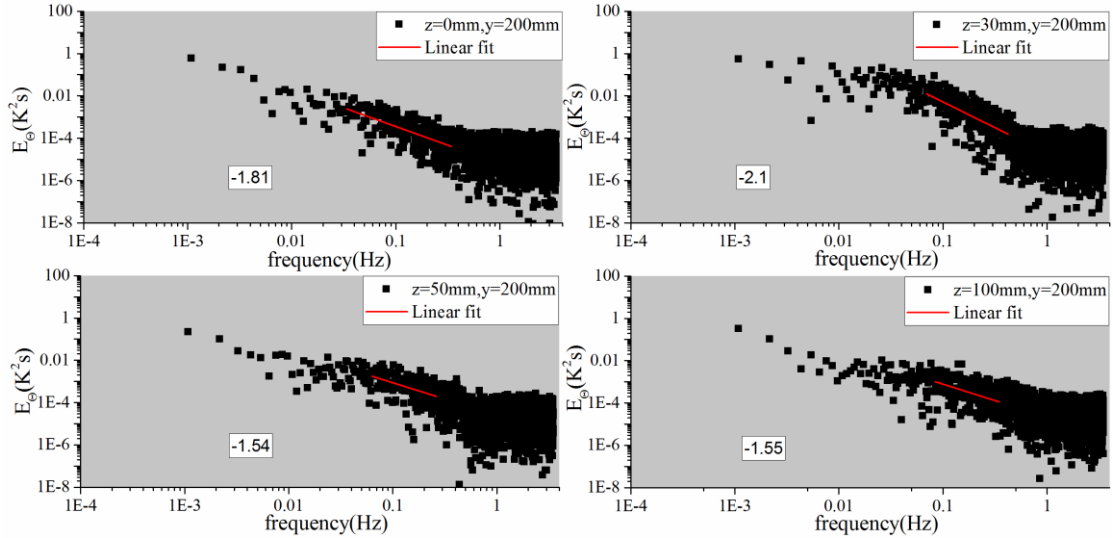
Fig. 17. Power spectrum of temperature of the points that are 0mm, 30mm, 50mm and 100mm away from the vertical surface

Although the dimension and shape of the heating unit in this study are somewhat different

from those of actual radiator, the heat transfer process of the heating unit is similar to that of an

actual radiator under full scale room conditions. The influence of the surface temperature of the

heating unit and the mechanical ventilation on the thermodynamic state of the near-wall airflow

543   over the heating unit found in this study can be referred in the research of actual heating room. In

544   addition, TIV is proved to be feasible in the measurement of the near-wall airflow over a heating

545   unit and can be used as an alternative indoor velocity measurement method to make up for the fact

546   that it is difficult to use PIV in full scale measurements. Based on the measurement and analyzing

547   method, future work can be carried out to investigate the thermodynamic state of the airflow over

548   a radiator in a full scale room environment.

549   **5. Conclusions**

550   This paper analyzed the thermodynamic state of the near-wall airflow over an idealized

551   heating unit. The air temperature was measured by RTDs, and the near-wall velocity distributions

552   were measured by the PIV method and TIV method. By analyzing the temperature and velocity

553   measurement results, the following conclusions can be drawn:

554   (a) Overall, TIV and PIV8 are close and consistent in magnitude and trend. TIV has certain

555   feasibility in reflecting the spatial distribution characteristics of the near-wall airflow in

556   both natural convection and mixed convection. The spectral shapes of TIV and PIV fit

557   well in low-frequency regions. The great fitness in the low-frequency region means that

558   the measurement results of TIV can reflect the main flow characteristics of turbulent

559   flow motion. TIV can be used to obtain the near-wall velocity according to the wall

560   surface temperature fluctuations and the obtained velocity is closely associated with the

561   boundary layer. Due to the heat storage of the vertical wall, lag exists between the

562   surface temperature fluctuation and the near-wall velocity fluctuation.

563   (b) Influenced by thermal buoyancy, the near-wall velocity over the heating unit in natural

564   convection case shows vertical variation. With an increase in heating temperature, the

565   velocity distribution exhibits a more pronounced spatial difference in the vertical

566   direction, and the position at which the maximum velocity occurs moves upward.

567   Correspondingly, the value of the maximum velocity increases with an increase in

568   heating temperature as well. The flow under natural convection cases is in fully

569   developed turbulent, and the flow state of mixed convection is influenced by the

570   characteristics of supply air. The influence of mechanical ventilation is far stronger than

571   that of natural convection in mixed convection case, and as the vertical distance from the

572   air inlet increases, the air velocity gradually decreases.

573   (c) The temperature fluctuation near the vertical surface is large at locations within 30 mm

574   away from the vertical surface. The temperature of the air near the vertical wall has a

575   significant influence on the heat transfer rate of the vertical wall. With an increase in

576   heating temperature, the air and surface temperature gradients increase, especially those

577   near the vertical surface. Accordingly, the near-wall heat transfer rate of the vertical wall

578   increases as well. Under the effect of mechanical ventilation, the air and surface

579   temperatures decrease and tend to be more uniform, and the temperature gradient is

580   reduced. The heat transfer rate of the vertical wall decreases. Due to an insufficient of

581   driving force, there exists a temperature detachment over the heating unit. Influenced by

582   mechanical ventilation, the detachment position of the mixed convection case is higher

583   than those of the natural convection cases.

587   **References**

588   [1]   J.A. Myhren, S. Holmberg, Performance evaluation of ventilation radiators, Appl. Therm.
589   Eng. 51 (2013) 315–324. doi:10.1016/j.applthermaleng.2012.08.030.
590   [2]   J.A. Myhren, S. Holmberg, Design considerations with ventilation-radiators: Comparisons to
591   traditional two-panel radiators, 41 (2009) 92–100. doi:10.1016/j.enbuild.2008.07.014.
592   [3]   G. Sevilgen, M. Kilic, Numerical analysis of air flow , heat transfer , moisture transport and
593   thermal comfort in a room heated by two-panel radiators, 43 (2011) 137–146.
594   doi:10.1016/j.enbuild.2010.08.034.
595   [4]   A. Jahanbin, E. Zanchini, Effects of position and temperature-gradient direction on the
596   performance of a thin plane radiator, Appl. Therm. Eng. 105 (2016) 467–473.
597   doi:10.1016/j.applthermaleng.2016.03.018.
598   [5]   W. Zhao, Y. Hu, Y. Wang, W. Qin, Thermal performance of a suspended ceiling fi n heat
599   transfer   panel   with   drain   pan,   Build.   Environ.   144   (2018)   622–630.
600   doi:10.1016/j.buildenv.2018.09.004.
601   [6]   Y. Lyu, X. Wu, C. Li, H. Su, L. He, Numerical analysis on the effectiveness of warm water
602   supply in water flow window for room heating, Sol. Energy. 177 (2019) 347–354.
603   doi:10.1016/j.solener.2018.11.033.
604   [7]   S. Xu, R. Ding, J. Niu, G. Ma, Investigation of air-source heat pump using heat pipes as heat
605   radiator, Int. J. Refrig. 90 (2018) 91–98. doi:10.1016/j.ijrefrig.2018.03.025.
606   [8]   H.B. Awbi, A. Hatton, Natural convection from heated room surfaces, Energy Build. 30
607   (1999) 233–244.
608   [9]   T. Cholewa, R. Anasiewicz, A. Siuta-Olcha, M.A. Skwarczynski, On the heat transfer
609   coefficients between heated/cooled radiant ceiling and room, Appl. Therm. Eng. 117 (2017)
610   76–84. doi:10.1016/j.applthermaleng.2017.02.019.
611   [10]   Y. Sun, Y. Zhang, An Overview of Room Air Motion Measurement: Technology and
612   Application, HVAC&R Res. 13 (2007) 929–950. doi:10.1080/10789669.2007.10391463.
613   [11]   S. Fu, P.H. Biwole, C. Mathis, Particle tracking velocimetry for indoor airflow field: A review,
614   Build. Environ. 87 (2015) 34–44. doi:10.1016/j.buildenv.2015.01.014.
615   [12]   C. Cierpka, R. Hain, N.A. Buchmann, Flow visualization by mobile phone cameras, Exp.
616   Fluids. 57 (2016). doi:10.1007/s00348-016-2192-y.
617   [13]   A. Sattari, Particle image velocimetry visualization and measurement of airflow over a
618   wall-mounted   radiator,   Int.   J.   Vent.   14   (2015)   289–302.
619   doi:10.1080/14733315.2015.11684087.
620   [14]   W. Du, Y. Liu, H. Yuan, S. Qiao, S. Tan, Experimental investigation on natural convection
621   and thermal stratification of IRWST using PIV measurement, Int. J. Heat Mass Transf. 136
622   (2019) 128–145. doi:10.1016/j.ijheatmasstransfer.2019.01.067.
623   [15]   Q. Wu, C. an Zhu, L. Liu, J. Liu, Z. Luo, Two-dimensional flow visualization and velocity
624   measurement in natural convection near indoor heated surfaces using a thermal image

625 velocimetry method, Appl. Therm. Eng. 146 (2019) 556–568.
626 doi:10.1016/j.applthermaleng.2018.10.023.

627 [16] W. Gao, R.H. Shaw, K.T. Paw U, Observation of organized structure in turbulent flow within
628 and above a forest canopy, Boundary-Layer Meteorol. 47 (1989) 349–377.
629 doi:10.1007/BF00122339.

630 [17] F. Castellví, C. Cammalleri, G. Ciraolo, F. Rossi, Daytime sensible heat flux estimation over
631 heterogeneous surfaces using multitemporal land-surface temperature observations. Water
632 Resour. Res. 52 (2016) 3457–3476.

633 [18] G.M. Carlomagno, G. Cardone, Infrared thermography for convective heat transfer
634 measurements, 2010. doi:10.1007/s00348-010-0912-2.

635 [19] M. Aminzadeh, D. Breitenstein, D. Or, Characteristics of Turbulent Airflow Deduced from
636 Rapid Surface Thermal Fluctuations: An Infrared Surface Anemometer, Boundary-Layer
637 Meteorol. (2017) 1–16. doi:10.1007/s10546-017-0279-5.

638 [20] E. Haghighi, D. Or, Thermal signatures of turbulent airflows interacting with evaporating thin
639 porous surfaces, Int. J. Heat Mass Transf. 87 (2015) 429–446.

640 [21] C.J. Legleiter, P.J. Kinzel, J.M. Nelson, Remote measurement of river discharge using
641 thermal particle image velocimetry (PIV) and various sources of bathymetric information, J.
642 Hydrol. 554 (2017) 490–506. doi:10.1016/j.jhydrol.2017.09.004.

643 [22] T. Lopez, H.E. Thomas, A.J. Prata, A. Amigo, D. Fee, D. Moriano, Volcanic plume
644 characteristics determined using an infrared imaging camera, J. Volcanol. Geotherm. Res. 300
645 (2014) 148–166. doi:10.1016/j.jvolgeores.2014.12.009.

646 [23] A. Tiddens, K. Risthaus, M. Röger, H. Stadler, B. Hoffschmidt, Induced Infrared
647 Thermography: Flow visualizations under the extreme conditions of an open volumetric
648 receiver of a solar tower, Int. J. Heat Fluid Flow. 65 (2017) 105–113.
649 doi:10.1016/j.ijheatfluidflow.2017.04.002.

650 [24] Z.C. Huang, K.S. Hwang, Measurements of surface thermal structure, kinematics, and
651 turbulence of a large-scale solitary breaking wave using infrared imaging techniques, Coast.
652 Eng. 96 (2015) 132–147. doi:10.1016/j.coastaleng.2014.12.005.

653 [25] A. Inagaki, M. Kanda, S. Onomura, H. Kumemura, Thermal Image Velocimetry,
654 Boundary-Layer Meteorol. 149 (2013) 1–18. doi:10.1007/s10546-013-9832-z.

655 [26] Y. Fan, Y. Li, S. Yin, Non-uniform ground-level wind patterns in a heat dome over a
656 uniformly heated non-circular city, Int. J. Heat Mass Transf. 124 (2018) 233–246.
657 doi:10.1016/j.ijheatmasstransfer.2018.03.069.

658 [27] E. Lev, M. Spiegelman, R.J. Wysocki, J.A. Karson, Investigating lava flow rheology using
659 video analysis and numerical flow models, J. Volcanol. Geotherm. Res. 247–248 (2012)
660 62–73. doi:10.1016/j.jvolgeores.2012.08.002.

661 [28] A. Garai, J. Kleissl, Air and Surface Temperature Coupling in the Convective Atmospheric
662 Boundary Layer, J. Atmos. Sci. 68 (2011) 2945–2954. doi:10.1175/JAS-D-11-057.1.

663 [29] M. Katurji, P. Zawar-reza, Forward-Looking Infrared Cameras for Micrometeorological
664 Applications within Vineyards, Sensors. 16 (2016) 2–11. doi:10.3390/s16091518.

665 [30] A.M. Grudzielanek, J. Cermak, Capturing Cold-Air Flow Using Thermal Imaging,
666 Boundary-Layer Meteorol. 157 (2015) 321–332. doi:10.1007/s10546-015-0042-8.

667 [31] A. Koca, G. Cetin, Experimental investigation on the heat transfer coefficients of radiant
668 heating systems: Wall, ceiling and wall-ceiling integration, Energy Build. 148 (2017)

669   311–326. doi:10.1016/j.enbuild.2017.05.027.

670   [32] X. Zhang, G. Su, J. Yu, Z. Yao, F. He, PIV measurement and simulation of turbulent thermal
671   free convection over a small heat source in a large enclosed cavity, Build. Environ. 90 (2015)
672   105–113. doi:10.1016/j.buildenv.2015.03.015.

673   [33] H. Karatas, T. Derbentli, Natural convection and radiation in rectangular cavities with one
674   active vertical wall, Int. J. Therm. Sci. 123 (2018) 129–139.

675   [34] H. Karatas, T. Derbentli, Natural convection in rectangular cavities with one active vertical
676   wall, Int. J. Heat Mass Transf. 105 (2017) 305–315.

677   [35] H. Karatas, T. Derbentli, Three-dimensional natural convection and radiation in a rectangular
678   cavity with one active vertical wall, Exp. Therm. Fluid Sci. 88 (2017) 277–287.
679   doi:10.1016/j.expthermflusci.2017.05.025.

680   [36] TL. Bergman, AS. Lavine, FP. Incropera, DP. DeWitt, Fundamentals of Heat and Mass
681   Transfer: Seventh Edition, John Wiley & Sons, 2011.

682   [37] YF. Liu, ZY. Gao, XJ. Gao, Heat transfer, China Electric Power Press, 2015.

683   [38] G. Hetsroni, T.A. Kowalewski, B. Hu, A. Mosyak, Tracking of coherent thermal structures on
684   a heated wall by means of infrared thermography, 30 (2001) 286–294.

685   [39] Y. Cheng, Z. Lin, Experimental study of airflow characteristics of stratum ventilation in a
686   multi-occupant room with comparison to mixing ventilation and displacement ventilation,
687   Indoor Air. 25 (2015) 662–671. doi:10.1111/ina.12188.

688   [40] Q. Ouyang, W. Dai, H. Li, Y.Z. Ã, Study on dynamic characteristics of natural and
689   mechanical wind in built environment using spectral analysis, 41 (2006) 418–426..

690   [41] M. Lesieur. Turbulence in fluids, Springer, 2008.

691   [42] X. Zhang, J. Yu, G. Su, Z. Yao, P. Hao, F. He, Statistical analysis of turbulent thermal free
692   convection over a small heat source in a large enclosed cavity, Appl. Therm. Eng. 93 (2016)
693   446–455. doi:10.1016/j.applthermaleng.2015.10.011.